

Supervised convolutional network for three-dimensional fluid data reconstruction from sectional flow fields with adaptive super-resolution assistance

Mitsuaki Matsuo, Taichi Nakamura, Masaki Morimoto

Department of Mechanical Engineering, Keio University, Yokohama, 223-8522, Japan

Kai Fukami

Department of Mechanical and Aerospace Engineering, University of California, Los Angeles, CA 90095, USA

Department of Mechanical Engineering, Keio University, Yokohama, 223-8522, Japan

Koji Fukagata*

Department of Mechanical Engineering, Keio University, Yokohama, 223-8522, Japan

Abstract

The recent development of high-performance computing enables us to generate spatio-temporal high-resolution data of nonlinear dynamical systems and to analyze them for deeper understanding of their complex nature. This trend can be found in a wide range of science and engineering communities, which suggests that detailed investigations on efficient data handling in physical science must be required in future. To this end, we introduce the use of convolutional neural networks (CNNs) to achieve an efficient data storage and estimation of scientific big data derived from nonlinear dynamical systems.

The CNN is utilized to reconstruct three-dimensional data from a few numbers of two-dimensional sections in a computationally friendly manner. The present model is a combination of two- and three-dimensional CNNs, which allows users to save only some of the two-dimensional sections to reconstruct the volumetric data. As an example of three-dimensional data, we consider a fluid flow around a square cylinder at the diameter-based Reynolds number Re_D of 300, and show that volumetric fluid flow data can successfully be reconstructed with the present method from as few as five sections. Furthermore, we also propose a combination of the present CNN-based reconstruction with an adaptive sampling-based super-resolution analysis to augment the data compression capability of the present methods. Our report can be a significant bridge toward practical data handling for not only the fluid mechanics field but also a vast range of physical sciences.

Keywords: Convolutional neural network, wake, volumetric reconstruction, super resolution

*Corresponding author

Email address: fukagata@mech.keio.ac.jp (Koji Fukagata)

1. Introduction

Scientific big data has recently been accumulated due to the improvement in computational power following Moore’s law [1]. These trends owing to high-performance computing enable us to notice that detailed investigations on big data handling must be helpful for a wide range of scientific community in future from the perspective of efficient storage and exchange of data. In this paper, we consider a supervised machine-learning-based method to achieve an efficient data handling of scientific big data derived from nonlinear dynamical systems with an example of fluid flows.

Fluid flow data can be regarded as one of the examples of big data derived from complex physics which contains strong nonlinearities and spatio-temporal multi-scale nature. Due to such natures, large-scale numerical simulations are often required for detailed analyses. For example, let us consider the use of direct numerical simulation (DNS) over an arbitrary three-dimensional domain discretized with 100 points in each direction — the sum of data points reaches 4-million dimension since there are three velocity components ($\mathbf{u} = \{u, v, w\}$) and pressure for all computational points of 100^3 . We hope you can now feel its unbelievable number with this simple example. In fact, the number of grid points contained in the data used in this study is much greater than this example. Besides, it has also widely been known that the requirement for the number of computational grid points for DNS is usually in proportion to $Re^{9/4}$, where Re is the Reynolds number, which makes us encounter the challenges due to the limitation of computational power [2].

To handle the high-dimensional complex fluid flow data in an efficient manner, the utilization of machine learning (ML) has been attracting attention as a powerful tool [3, 4]. The ML is good at handling them by accounting nonlinearities into its procedure [5]. We can see the great potential of ML methods from the perspectives on both reduced-order modeling (ROM) [6] and data estimation [7]. For instance, an autoencoder (AE) [8], a neural-network-based low dimensionalization tool, can be regarded as the notable ROM effort with ML for fluid flow data analyses [9]. The AE has a bottleneck structure and is trained by setting the same data for both input and output. If the network is able to output the same data as the input, it implies that the high-dimensional original input or output can successfully be compressed into the bottleneck space referred to as the latent space. This idea has widely been accepted in the fluid dynamics community [10, 11, 12, 13, 14, 15, 16, 17, 18, 19, 20, 21, 22, 23, 24]. Regarding the data estimation, the success of a global flow field estimation from local sensor measurements [25, 26] or low-resolution data [27, 28, 29] indicates the possibility that we only need to keep these input data of their problem settings and ML models to represent the high-dimensional original data. However, there are few studies for three-dimensional fluid data estimation or low dimensionalization despite the demands for a detailed investigation from the perspective on efficient data handling as introduced above.

Motivated by the aforementioned backgrounds, we introduce an efficient data handling method by considering fluid flow examples. More concretely, we capitalize on a convolutional neural network (CNN) to reconstruct three-dimensional spatial discretized data from a few numbers of two-dimensional sections. As an example of three-dimensional data, a flow around a square cylinder at the Reynolds number $Re_D = 300$ is considered. In addition, we also propose the combination with an adaptive sampling-based super-resolution analysis, which reconstructs a high-resolution flow field from its low-resolution counterpart, to achieve much more efficient data handling for complex fluid flows. The

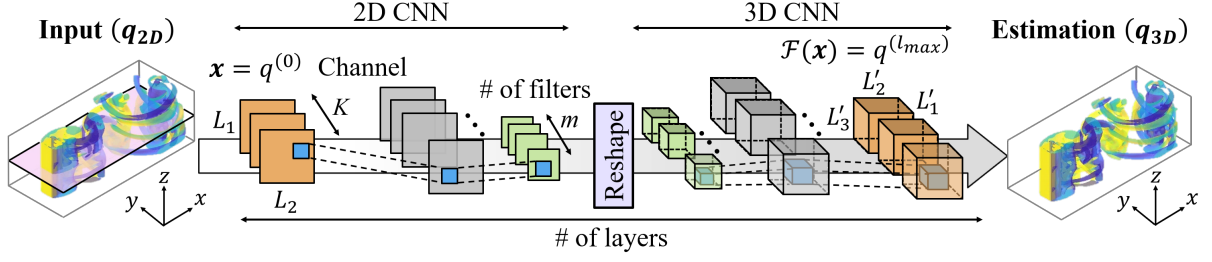


Figure 1: 2D-3D CNN utilized in this study. Input cross-sectional data is converted to three-dimensional volumetric data via two-dimensional and three-dimensional convolutional neural network.

idea of the adaptive sampling here enables us to save low-resolution flow data in a computationally efficient manner by focusing on an important portion on a fluid flow field. The present paper is organized as follows: schemes of machine learning and proposed adaptive sampling are summarized in section 2. Results with discussions are offered in section 3. We finally provide concluding remarks with expected outlooks of machine-learning-based data handling for nonlinear dynamical systems including the fluid mechanics, in section 4.

2. Methods

2.1. 2D-3D convolutional neural networks

We utilize a convolutional neural network (CNN) [30] to reconstruct the three-dimensional flow data. The CNN excels at extracting features from a large amount of data thanks to its filter operator, and it has been utilized in image processing and classification tasks [31]. In the field of fluid dynamics, the use of CNN is also spreading because the filter shearing allows us to handle the high-dimensional fluid data efficiently [32, 33, 34, 35, 36].

The present idea is founded on a combination of two- and three-dimensional CNN to obtain a three-dimensional output from two-dimensional input, as shown in figure 1. The two-dimensional CNN is composed of two-dimensional convolutional layers and max pooling layers. The convolutional layer is used to extract the feature of two-dimensional sections, while we can reduce the dimension of the data with the max pooling layers. The use of a dimensional reduction tool for this part is vital for the CNN-based data reconstruction to obtain the robustness against the rotation and translation of the images and noisy inputs [37], although the model eventually aims to reconstruct the higher dimension data. As shown in figure 1, the three-dimensional layers are in charge of dimension extension. Through the internal procedure of two-dimensional convolutional layer illustrated in figure 2(a), the output $x^{(\iota)}$ at the layer ι , location (i, j) , and filter index m , can be generated. Namely, the output $x^{(\iota)}$ can be expressed as

$$x_{ijm}^{(\iota)} = \varphi \left(b_m^{(\iota)} + \sum_{l=0}^{L-1} \sum_{p=0}^{H-1} \sum_{q=0}^{H-1} h_{pqlm}^{(\iota)} x_{i+p-G, j+q-G, l}^{(\iota-1)} \right), \quad (1)$$

where $G = \text{floor}(H/2)$, K is the number of channels in a convolution layer, b_m is the bias, and φ is an activation function. As the activation function φ , we use a ReLU function [38]

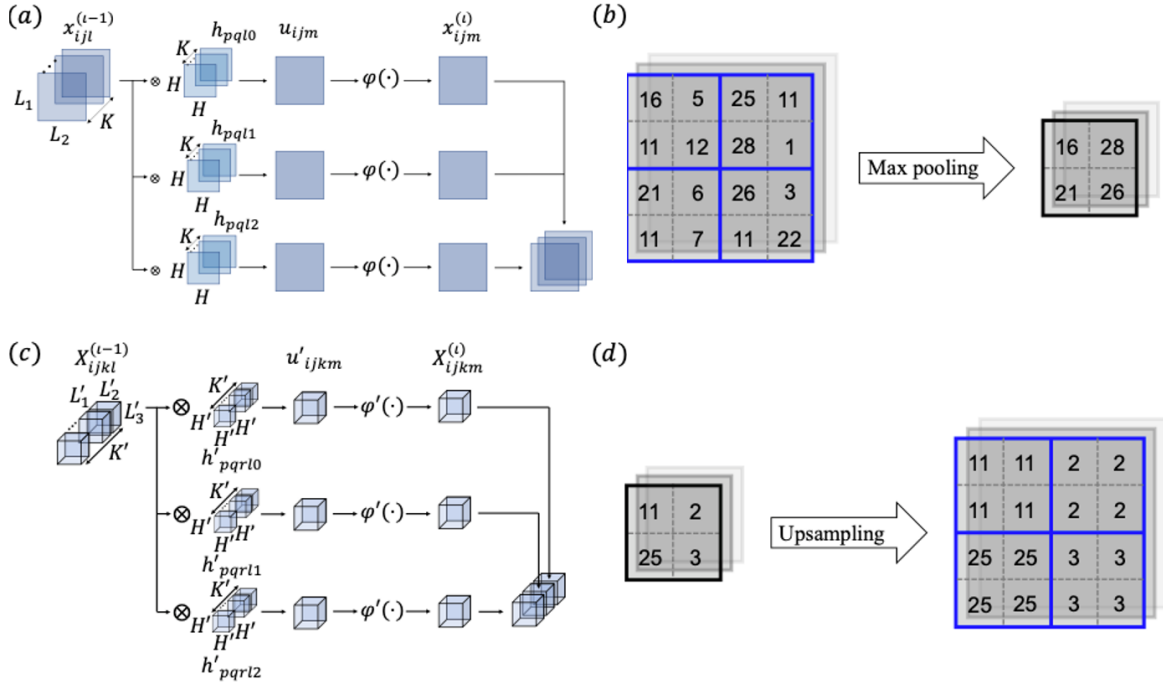


Figure 2: Internal procedure of convolutional neural network. (a) Two-dimensional convolution operation. (b) Max pooling. (c) Three-dimensional convolution operation. (d) Upsampling. We use two-dimensional examples for (c) and (d) for clarity of illustration.

to avoid vanishing gradients. As mentioned above, we also consider a max pooling layer shown in figure 2(b) to achieve the robustness against rotation and translation of images.

The extracted feature vectors through the two-dimensional CNN operations are given to the three-dimensional CNN, which includes the convolutional layer and an upsampling layer, for heading to the output layer. The internal procedure of three-dimensional convolutional layer is illustrated in figure 2(c). Here, the output $X^{(t)}$ at the layer t , location (i, j, k) , and filter index m , can be generated by convolutional operation $h'^{(t)}$. The output $X^{(t)}$ can be represented as

$$X_{ijkm}^{(t)} = \varphi' \left(b_m'^{(t)} + \sum_{l=0}^{L'-1} \sum_{p=0}^{H'-1} \sum_{q=0}^{H'-1} \sum_{r=0}^{H'-1} h'_{pqrlm}{}^{(t)} X_{i+p-G', j+q-G', k+r-G', l}^{(t-1)} \right), \quad (2)$$

where $G' = \text{floor}(H'/2)$, K' is the number of channels, b_m' is the bias, and φ' is an activation function, which is analogous to the two-dimensional operation in equation 1. The upsampling layer illustrated in figure 2(d) plays a role of dimension extension.

The details of the proposed model are summarized in Table 1. As the input and output attributes, we use three velocity components $\mathbf{q} = \{u, v, w\}$. The features of input sectional data \mathbf{q}_{2D} are extracted through two-dimensional convolutional layers and reduced in dimension by max pooling layer. Since it is widely known the pooling operations enable CNN models to acquire robustness against the variance of input data due to a decrease of spatial sensitivity [30], we here consider a maxpooling operation as noted as “1st Max Pooling” in Table 1. Once data shape is converted for three-dimensional convolutional

Table 1: The network structure of 2D-3D CNN. The convolution layer is denoted as Conv.

Layer (filter size, # of filters)	Data size	Activation
Input	$(256, 128, 3 \times n_{\text{section}})$	
1st Conv2D (3,32)	$(256, 128, 32)$	ReLU
2nd Conv2D (3,32)	$(256, 128, 32)$	ReLU
1st Max Pooling	$(128, 64, 32)$	
3rd Conv2D (3,16)	$(128, 64, 16)$	ReLU
4th Conv2D (3,20)	$(128, 64, 20)$	ReLU
Reshape	$(128, 64, 20, 1)$	
1st Conv3D (3,16)	$(128, 64, 20, 16)$	ReLU
2nd Conv3D (3,16)	$(128, 64, 20, 16)$	ReLU
1st Up-sampling	$(256, 128, 160, 16)$	
3th Conv3D (3,32)	$(256, 128, 160, 32)$	ReLU
4th Conv3D (3,32)	$(256, 128, 160, 32)$	ReLU
5th Conv3D (3,3)	$(256, 128, 160, 3)$	Linear

layers at the “Reshape” layer, the data head to the output layer. The output \mathbf{q}_{3D} is finally obtained via three-dimensional convolutional layers and upsampling. Note that users can also consider the use of optimization tools for the parameter decision inside CNNs, e.g., hyperopt [39] and Bayesian optimization [40].

The 2D-3D CNN model \mathcal{F} in the present study is trained in a supervised learning manner to obtain the three-dimensional data \mathbf{q}_{3D} from the input sectional data \mathbf{q}_{2D} . Therefore, the problem setting in this study results in an optimization problem,

$$\mathbf{w} = \operatorname{argmin}_{\mathbf{w}} \|\mathbf{q}_{3D} - \mathcal{F}(\mathbf{q}_{2D}; \mathbf{w})\|_2, \quad (3)$$

where \mathbf{w} is weights inside the present CNN. The L_2 error is applied as the loss function in equation 3. For the construction of the present model, we take an early stopping criterion [41] with 20 iterations to avoid an overfitting [42].

2.2. Super-resolution reconstruction with adaptive sampling

In this study, we will also unify the present 2D-3D convolutional neural network with the super-resolution analysis. More concretely, a machine learning model \mathcal{G} , which is distinct against the model for three-dimensional reconstruction \mathcal{F} , is utilized to reconstruct two-dimensional high-resolution sections $\mathbf{q}_{2D,HR}$ from their two-dimensional low-resolution counterparts $\mathbf{q}_{2D,LR}$. The super-resolved two-dimensional sections $\mathbf{q}_{2D,HR}$ are then fed into the model for three-dimensional reconstruction \mathcal{F} . The procedure can be mathematically expressed as

$$\mathbf{q}_{2D,HR} = \mathcal{G}(\mathbf{q}_{2D,LR}; \mathbf{w}_{\mathcal{G}}), \quad \mathbf{q}_{3D} = \mathcal{F}(\mathbf{q}_{2D,HR}; \mathbf{w}), \quad (4)$$

where $\mathbf{w}_{\mathcal{G}}$ denotes the weights inside the super-resolution model \mathcal{G} . This idea enables us to achieve much better data compression than cases without utilizing the super resolution because we need to save only two-dimensional low-resolution data.

To perform the super-resolution analysis, low-resolution data must be prepared for a training phase. They are usually generated through pooling operations which extracts

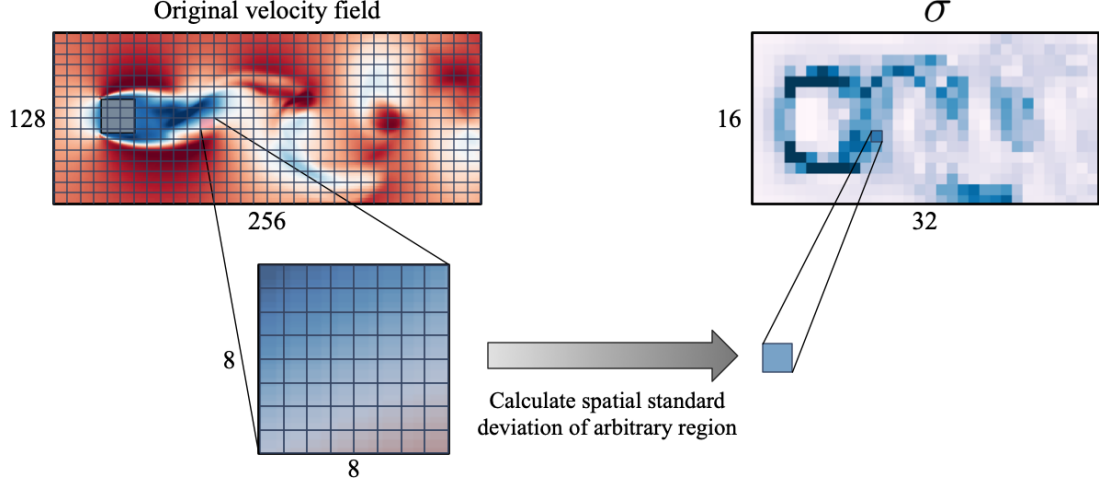


Figure 3: Generation of a standard deviation map from velocity data. An arbitrary area of $N_{sw} \times N_{sh} = 8 \times 8$ is considered to calculate the spatial standard deviation.

a representative value (max/average) from an arbitrary area [27]. With this pooling operations, the fluid data can be downsampled uniformly over the field. Although this is a simple and fast method to prepare low-resolution data, this may be an inefficient manner for some regions because the complexity varies in space. Therefore, in this study, we focus on the spatial standard deviation in each arbitrary sub-domain to determine the local degree of downsampling by accounting for the ‘importance’ of the data into a pooling process so as to make low-resolution data efficiently, referred to as *adaptive sampling*.

The detailed procedure of adaptive sampling is as follows. We first divide a velocity snapshot into small subdomains of $N_{sw} \times N_{sh}$, where N_{sw} and N_{sh} correspond to the width and the height of the sub-domain, respectively, as shown in figure 3. Then the spatial standard deviation of each sub-domain is calculated. Note that we do not take the standard deviation over time, but over each instantaneous snapshot to adapt the pooling procedure for each snapshot. Thus, as shown in figure 3, the map of spatial standard deviation can be generated with the size of $N_{\sigma,w} \times N_{\sigma,h}$, where $N_{\sigma,w} = N_x/N_{sw}$ and $N_{\sigma,h} = N_y/N_{sh}$, and $N_x \times N_y$ indicates the size of the entire cross section.

Utilizing the standard deviation map, we make the adaptive sampling-based low-resolution data with the local pooling rate α . Put simply, the adaptive sampling rate α decides how much we retain our data following the standard deviation map which represents the strong feature (i.e., strong color in figure 3) on each snapshot. The detailed procedure of adaptive sampling is as follows.

1. We first prepare a standard deviation map and find the portion with smaller values than a certain threshold, i.e., $\sigma_{i,j} < \gamma_{th,1}$.
2. We then scan the portions surrounding $\sigma_{i,j}$, i.e., $\{\sigma_{i+1,j}, \sigma_{i+2,j}, \dots, \sigma_{i+(\alpha_1/N_{sw}-1), j+(\alpha_1/N_{sh}-1)}\}$. If all the portions have smaller standard deviations than $\gamma_{th,1}$, we then take the pooling operation over $\sigma_{i,j}$ to $\sigma_{i+(\alpha_1/N_{sw}-1), j+(\alpha_1/N_{sh}-1)}$.
3. Next, for remaining portion, we scan over the standard deviation map again for an arbitrary portion with a standard deviation between the thresholds $\gamma_{th,1} < \sigma_{ij} < \gamma_{th,2}$.

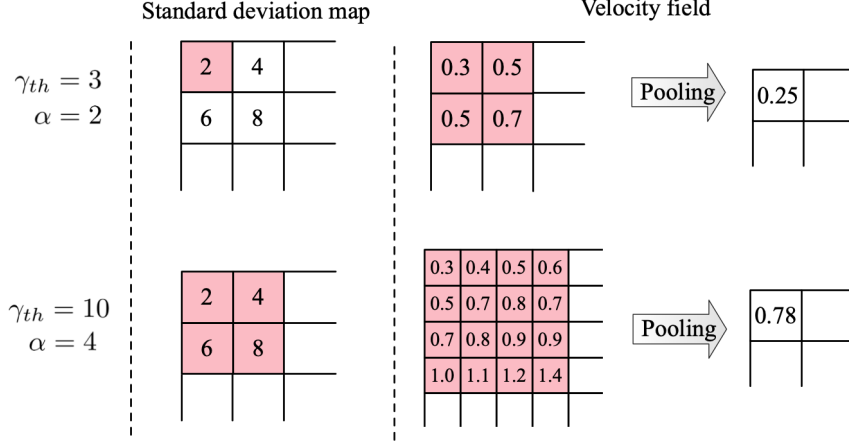


Figure 4: Adaptive sampling operation in this study.

4. Similarly, if the surrounding portion has thresholds less than $\gamma_{th,2}$, we take the pooling operation over $\sigma_{i,j}$ to $\sigma_{i+(\alpha_2/N_{sw}-1),j+(\alpha_2/N_{sh}-1)}$.
5. We finally take the standard average pooling operation for the remaining portions, where the standard deviation is higher than $\gamma_{th,2}$.

An illustrative example of the adaptive sampling operation is shown in figure 4. For example, let us focus on the case with $\gamma_{th} = 3$ and the pooling rate $\alpha = 2$. In this case, the pink region in the standard deviation map (where $\sigma = 2 < \gamma_{th}$) is only treated as the target region for the pooling operation. The region on the velocity field corresponding to the target region (having $\{0.3, 0.5, 0.5, 0.7\}$ with the size of 2×2) is then downsampled by using the average pooling. Consequently, we obtain 0.25 as the representative value as shown in figure 4. In sum, the downsampled velocity field at the region can be expressed with the data size of $1/\alpha^2$ ($= 25\%$) for the original data. Similarly, for the case with $\gamma_{th} = 10$ and $\alpha = 4$ illustrated in the lower part in figure 4, the target pooling region is expanded to the size of 4×4 having $\{2, 4, 6, 8\}$. In this case, the velocity field can be downsampled by $1/\alpha^2$ ($= 6.25\%$) for the original size. In other words, the portions having small standard deviations are discarded through the present operation — in turn, we can retain the region with a larger standard deviation where represents the strong feature of the velocity field. In the present study, we use the pooling rates $\{\alpha_1, \alpha_2, \alpha_3\} = \{32, 16, 8\}$.

The application of the aforementioned idea to the velocity field is presented in figure 5. As we can expect, the region with the higher spatial standard deviation corresponding to the shear layer of wake provides the higher resolution than that with the less spatial variation region. Note that we have the variation for the domain size among the same pooling rate since we consider the non-uniform grid in the y direction. In section 3.2, we will examine the applicability of proposed adaptive sampling in handling fluid flow data.

3. Results

We consider a flow around a square cylinder at Reynolds number $Re_D = 300$ as an example. Note in passing that this data can be regarded as a good example for the present study, since the flow at $Re_D = 300$ contains the complex three-dimensional structure

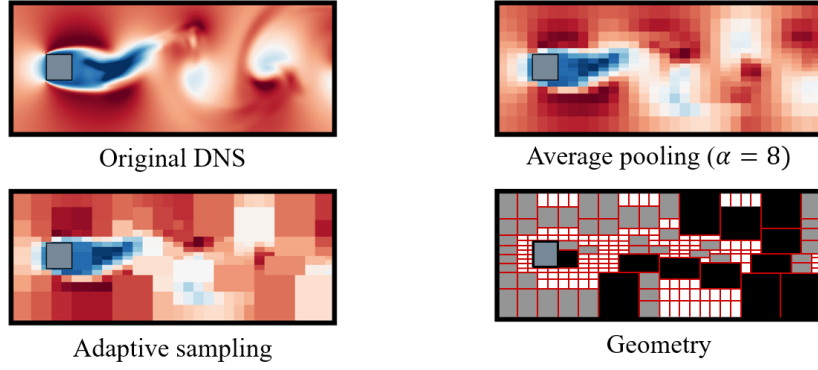


Figure 5: Application of the adaptive sampling to the present velocity field. For comparison, the standard average pooling with $\alpha = 8$ is also shown. The colors in the geometry image indicate the pooling rate α ; white represents $\alpha = 8$, gray represents 16 and black represents 32.

caused by a merge of both two- and three-dimensional separated shear layers [43]. The data set is prepared by direct numerical simulation (DNS) with numerically solving of the incompressible Navier–Stokes equations with a penalization term [44],

$$\nabla \cdot \mathbf{u} = 0, \quad \partial_t \mathbf{u} + \nabla \cdot (\mathbf{u}\mathbf{u}) = -\nabla p + Re_D^{-1} \nabla^2 \mathbf{u} + \lambda \chi (\mathbf{u}_b - \mathbf{u}), \quad (5)$$

where $\mathbf{u} = \{u, v, w\}$ and p are the velocity vector and pressure, respectively, nondimensionalized by the fluid density ρ , the length of the square cylinder D , and the uniform velocity U_∞ . The penalization term is utilized to express the body with a penalty parameter λ , a mask value χ , and a virtual velocity vector of a flow inside the object \mathbf{u}_b which is 0. The mask value χ is 0 outside an body and 1 inside an body. The computational domain is set to $(L_x \times L_y \times L_z) = (20D \times 20D \times 4D)$ and the computational time step is $\Delta t = 2.5 \times 10^{-3}$. A uniform velocity is imposed at the inflow boundary ($x = 0$), the convective boundary condition is adopted at the outflow boundary ($x = L_x$), the slip boundary condition is applied at $y = 0$ and $y = L_y$, and the periodic boundary condition is assumed at $z = 0$ and $z = L_z$. The center of the square cylinder is located $5.5D$ from the inflow boundary.

In this study, our focus is the part of computational volume around the square cylinder such that $(12.8D \times 4D \times 4D)$ with grid number of $(N_x^\sharp \times N_y^\sharp \times N_z^\sharp) = (256 \times 128 \times 160)$. We use 1000 snapshots for training the baseline model, although the dependence of the reconstruction ability on the amount of training snapshots will be investigated later.

Hereafter, we assess a three-dimensional reconstructed field from high-resolution two-dimensional velocity field data prepared by the DNS in section 3.1. We also discuss the possibility for more efficient data compression and reconstruction using a combination with the super-resolution concept in section 3.2.

3.1. Three-dimensional reconstruction from high-resolution two-dimensional sections

We first attempt to reconstruct a three-dimensional velocity field from two-dimensional high-resolution cross sections. In this study, four different number of input sections $n_{\text{section}} = \{1, 3, 5, 7\}$ are considered as illustrated in figure 6. Here, we place the baseline input section corresponding to $n_{\text{section}} = 1$ at the middle of the z direction. Three or more input sections are added with equal intervals in the z direction.

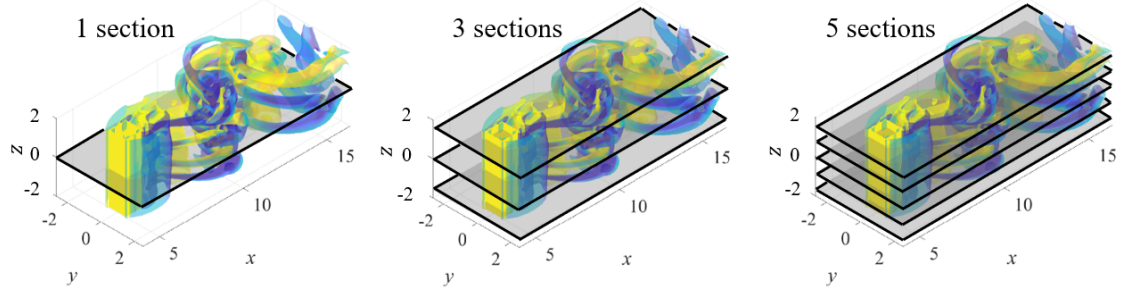


Figure 6: Concept of input location choice.

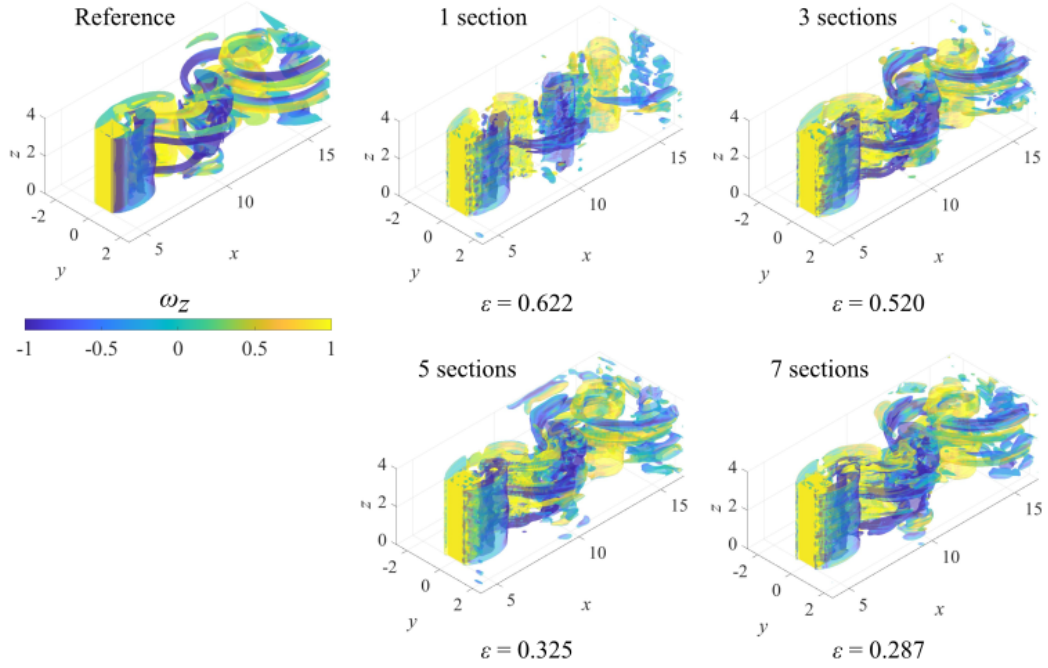


Figure 7: Convolutional neural network-based three-dimensional velocity field reconstruction fields using 1, 3, 5 and 7 cross sections (vortical structures identified by $\lambda_2 = -0.001$ and colored by the spanwise vorticity ω_z). The values underneath each subfigure indicates the ensemble L_2 error norm over all velocity attributes.

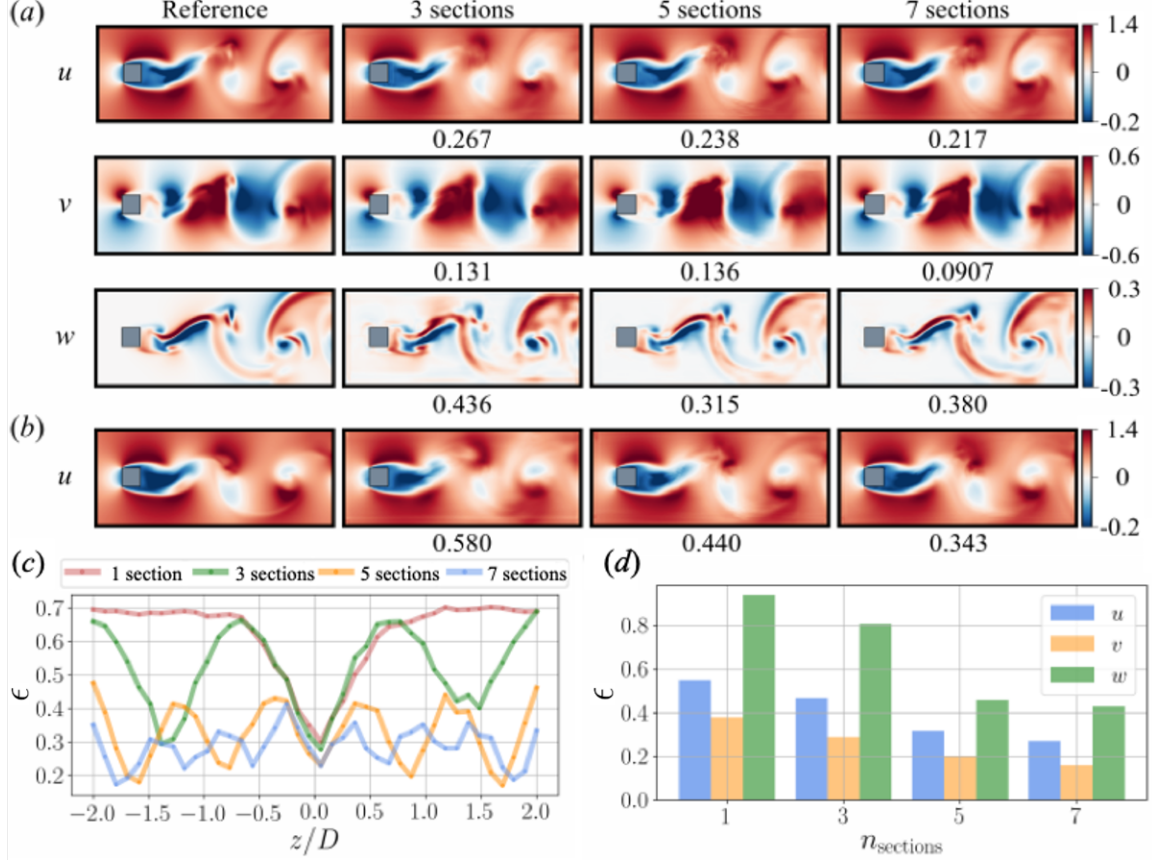


Figure 8: Details on convolutional neural network-based three-dimensional data reconstruction from two-dimensional sections. (a) Reconstructed sectional velocities at $z/D = 0.025$. For comparison, the streamwise velocity field at (b) $z/D = -2$ is also shown. (c) Dependence of L_2 error norm on the location in the z direction. (d) Dependence of L_2 error norm on the velocity attributes and the number of sections.

Three-dimensional reconstructed fields are visualized in figure 7. We here use a λ_2 vortex criterion [45] with $\lambda_2 = -0.001$ to identify the vortical structures. The basic trend observed here is that the use of more input sections provides better wake reconstruction. Notably, the present method is able to estimate the large structure in the flow field even from one cross-section in a qualitative manner. The reconstructed fields from five or more input sections have detailed three-dimensional structures and show reasonable agreement with the reference DNS data. This can also be found through the ensemble L_2 error norms over the velocity attributes $\bar{\epsilon} = \|\mathbf{q}_{\text{DNS}} - \mathbf{q}_{\text{ML}}\|_2 / \|\mathbf{q}'_{\text{DNS}}\|_2$ shown underneath each subfigure.

To further investigate the details of the estimated velocity field, the sectional estimated velocity fields at $\Delta z = 0.025D$ away from the input section, which is relatively close to the input section, are summarized in figure 8(a). The present models can reconstruct the flow field with reasonable accuracy in terms of both the visualization and the L_2 error norms. Especially, the reconstructed fields with $n_{\text{section}} = 7$ capture the fine structures and are almost indistinguishable from the reference. For comparison, the estimated streamwise velocity fields at $\Delta z = -2D$ away from the input section, which is relatively far away from the input section, are also examined in figure 8(b). The all reconstructed fields are in

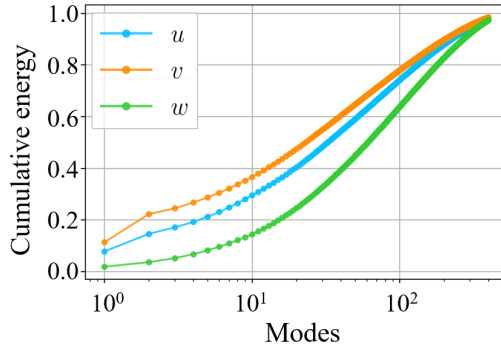


Figure 9: Singular value spectra of velocity fields.

qualitative agreement with the reference even at the edge of the reconstruction domain.

The discussion above focused on the results at the particular sections. Let us then evaluate the dependence of the L_2 error norm on the location in the z direction in figure 8(c). There are some valleys of the L_2 error near the input section, which makes sense since the ML is likely good at estimating fields near the input section. In addition, the error trends with a large number of input sections are entirely lower than those with the smaller numbers, which is attributed to the effect of multiple input sections.

We also summarize the relationship between the ensemble L_2 error norm over the domain for each velocity attribute and the number of input sections in figure 8(d). Similarly to figures 7 and 8(a) – (c), the larger n_{section} , the better reconstruction. It is also striking that we can see a significant difference in the estimation accuracy among velocity attributes — the L_2 error of v component reports much lower values than that of w component.

This difficulty for the w component coincides with Pérez et al. [46] who used a spatio-temporal Koopman decomposition for three-dimensional wake reconstruction around a square cylinder at $Re_D = 280$ from two-dimensional data. It can also be verified from the perspective on the data complexity of each attribute. We take the singular value decomposition (SVD) for snapshots of each velocity attribute, as presented in figure 9. As can clearly be found, the rate of energy accumulation for velocity w component is much slower than that of the other components. This example analysis implies that we may be able to relate the assessment of machine-learning-based estimation with linear analyses like SVD [47].

Let us examine the dependence of the estimation accuracy on the number of training snapshots, as presented in figure 10. For this investigation, we use $n_{\text{sections}} = 5$ for all models. The time interval among snapshots is fixed for all covered n_{snapshot} , which implies that the length of reference time over training data increases with n_{snapshot} while the temporal density among snapshots is the same for all models.

The error decreases with increasing the number of training snapshots. Interestingly, the present model trained with $n_{\text{snapshot}} = 50$ is able to capture large scale structures of the flow of the u and v components although the field of w component is blurry. This difference among velocity attributes can also be explained with their complexities observed in figure 9. With $n_{\text{snapshot}} \geq 300$, the present model can achieve a reasonable

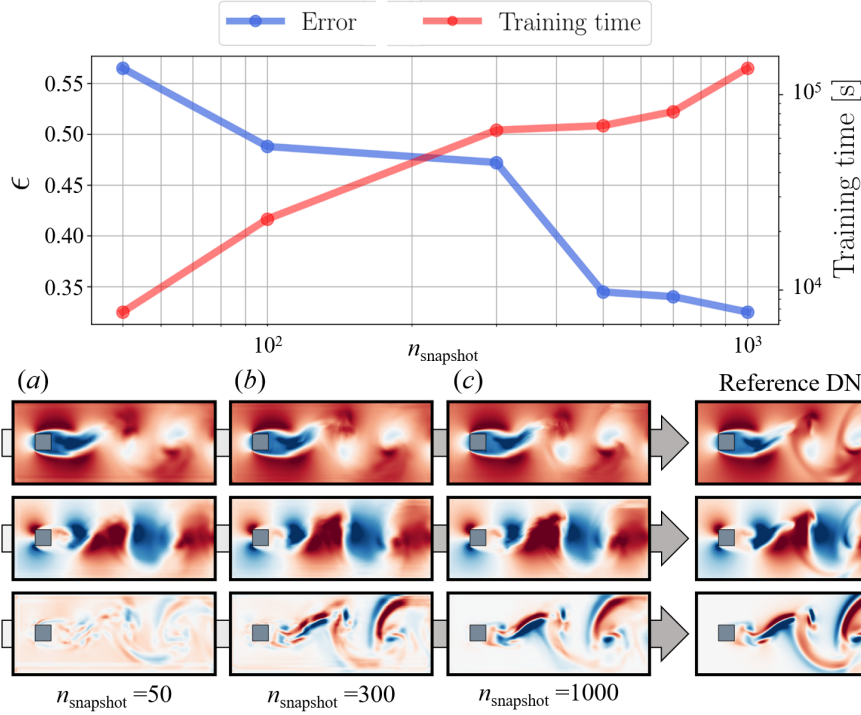


Figure 10: Dependence of estimation ability on the number of training snapshots and training time.

reconstruction. We also observe the computational cost for constructing the present models, as the red curve in figure 10. For instance, it takes approximately 38 hours on the NVIDIA TESLA V100 graphics processing unit (GPU) for the case with $n_{\text{snapshot}} = 1000$. Note that the increase of computational costs does not show the linear behavior because of the use of early stopping as mentioned above. Users should care about the trade-off relationship between the computational cost and the estimation accuracy depending on their requirements.

The aforementioned results enable us to have the expectation for the application of the present model to particle image velocimetry, e.g., estimation of whole flow field from two-dimensional sections that can only be measured due to experimental constraints. Hence, we also assess the robustness of the present model against noisy input. To determine the magnitude of given noise, we use the signal-noise ratio (SNR) as $\text{SNR} = \sigma_{\text{sensor}}^2 / \sigma_{\text{noise}}^2$, where σ_{sensor} and σ_{noise} represent variance of data and variance of noise, respectively. We test six cases of noise magnitudes as $1/\text{SNR} = \{0.001, 0.005, 0.01, 0.05, 0.1, 0.5\}$.

The investigation for the robustness against noisy input data is summarized in figure 11. We here use $n_{\text{sections}} = 5$. Up to $1/\text{SNR} = 0.01$, the estimation error is almost the same as that without noise. The estimated fields also show no significant difference against the reference DNS. However, with $1/\text{SNR} = 0.05$ or more, the estimated fields do not include finer structures in addition to the overestimation of their velocity magnitude.

3.2. Super-resolution aided efficient data handling

As introduced in 2.2, we seek the extensional possibility of the present method which estimates three-dimensional data from low-dimensional two-dimensional sectional data

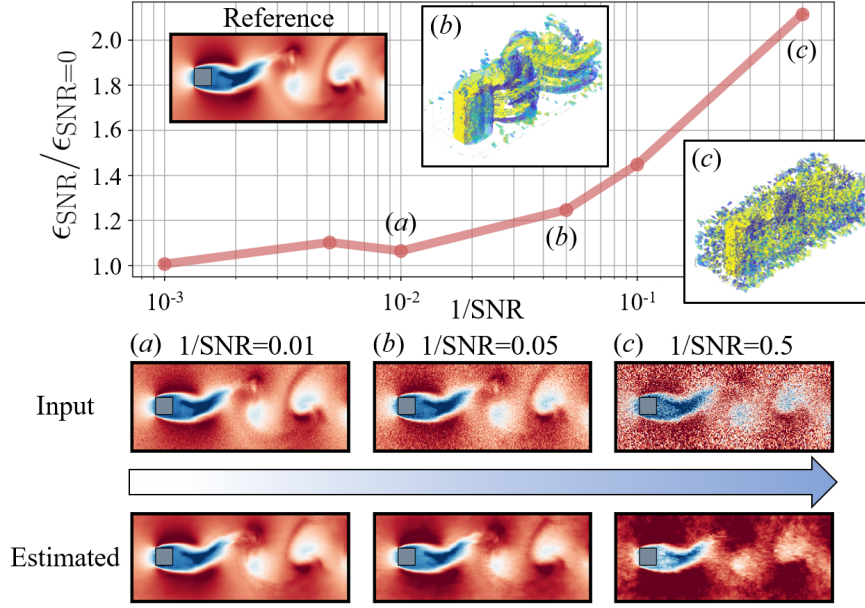


Figure 11: Robustness of the present model against noisy input.

by combining with super-resolution analysis toward more efficient data handling. Super resolution reconstructs high-resolution data from its low-resolution counterpart. Fukami et al. recently applied a CNN-based super resolution to fluid flow fields and reported its potential [27, 29]. Motivated by these studies, we here propose the combination of the present three-dimensional reconstruction with the super-resolution analysis as follows;

1. Two-dimensional high-resolution flow fields $\mathbf{q}_{2D,HR}$ are reconstructed from low-resolution counterparts $\mathbf{q}_{2D,LR}$ through the super resolution such that $\mathbf{q}_{2D,HR} = \mathcal{G}(\mathbf{q}_{2D,LR})$.
2. The super-resolved two-dimensional sections $\mathbf{q}_{2D,HR}$ are then utilized as the input for the model of three-dimensional reconstruction such that $\mathbf{q}_{3D} = \mathcal{F}(\mathbf{q}_{2D,HR})$.

This procedure allows us to save only low-resolution sectional flow fields $\mathbf{q}_{2D,LR}$ so as to represent the three-dimensional field \mathbf{q}_{3D} , as expressed in equation 4. As the machine learning model \mathcal{G} for super-resolution analysis, we use the two-dimensional CNN which contains 7 layers and 5×5 filters with ReLU activation function. Since the input low-resolution data is resized to the high-resolution image size before feeding into the model, the pooling or upsampling layers are not considered for the construction of model \mathcal{G} .

In what follows, we apply a normal super-resolution analysis with a conventional pooling operation in section 3.2.1. Moreover, we also examine the possibility of additional data saving with the super-resolution analysis by considering *adaptive sampling* in section 3.2.2.

3.2.1. Utilization of typical super resolution

Before combining with the present 2D-3D CNN, let us examine the super resolution of two-dimensional velocity fields itself. In this section, to generate low-resolution data,

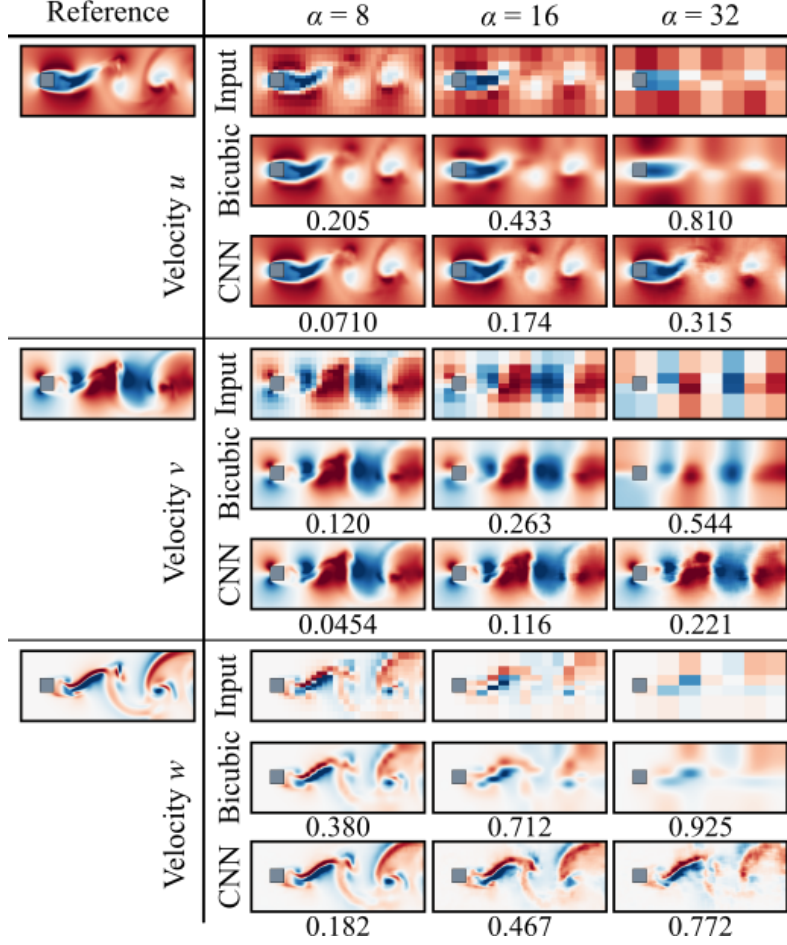


Figure 12: Super-resolution reconstruction for two-dimensional velocity fields. The values underneath the contours indicate the L_2 error norm ϵ . The contour level for each velocity attribute is the same as that used in figure 8.

we use an average pooling which extracts a mean value in an arbitrary area such that

$$\mathbf{q}_{ij,\text{LR}} = \frac{1}{\alpha^2} \sum_{p,s}^{\alpha} (\mathbf{q}_{psij,\text{HR}}), \quad (6)$$

where α denotes a downsampling factor. We consider three cases of downsampling factor $\alpha = 8, 16$, and 32 . We also compare to the bicubic interpolation which is a conventional method for super resolution [48].

We summarize the application of two-dimensional super resolution to the velocity fields in figure 12. As an overall trend, the machine-learned super resolution is superior to the bicubic interpolation in terms of estimation accuracy with all downsampling factors, which is similar to [27]. Although the bicubic interpolation shows reasonable reconstruction with $\alpha = 8$, this trend can clearly be seen with $\alpha = 16$ and 32 . The difference among velocity attributes is caused by their complexities as presented in figure 9.

We here compare the computational costs for training the machine learning model of super resolution and reconstructing a high-resolution field in table 2. The CNN can reconstruct a flow field as fast as the bicubic interpolation although it takes approximately

Table 2: Computational costs for super-resolution analysis. The computational times for training of the present two-dimensional CNN-based super resolution model with 1000 snapshots and reconstruction of one snapshot by the bicubic and the CNN are reported. We here use the low-resolution data with $\alpha = 8$.

	Bicubic	CNN
Training (h)	-	22.2
Reconstruction (s)	5.53×10^{-1}	5.41×10^{-1}

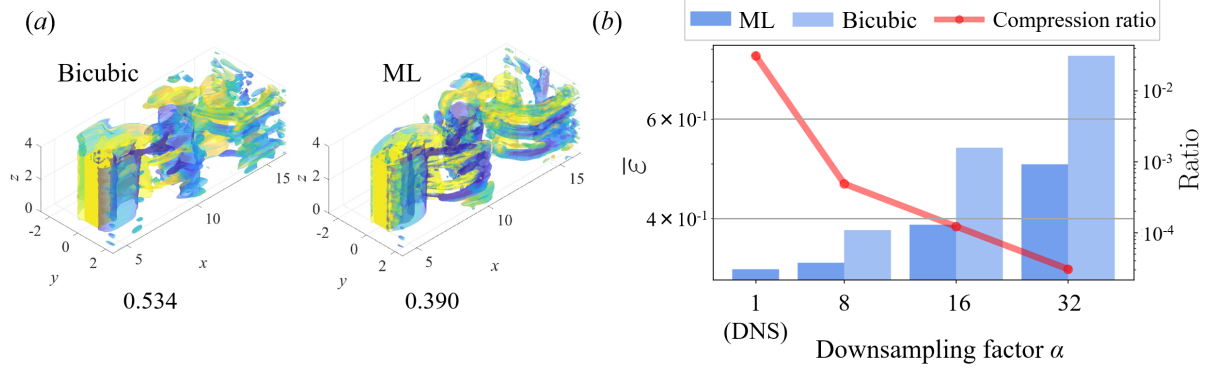


Figure 13: Three-dimensional reconstruction from the super-resolved two-dimensional data. (a) The reconstructed fields from the super-resolved sectional data by bicubic interpolation (left) and machine learning (right). Values underneath the three-dimensional isosurfaces indicate the L_2 error norm. (b) The relationship among the L_2 error norm, the compression ratio, and the downsampling factor α .

22 hours to train the machine learning model on the NVIDIA TESLA V100 graphics processing unit (GPU) with $n_{\text{snapshot}} = 1000$. But we should emphasize that the present machine-learned model can be used while achieving a better reconstruction with a reasonable estimation cost, once the training is successfully performed.

The super-resolved two-dimensional sectional data are then fed into the 2D-3D CNN. Here, we consider both the machine-learning-based super resolution and bicubic interpolation for the input. For the three-dimensional reconstruction model \mathcal{F} , we use $n_{\text{section}} = 5$. Three-dimensional reconstructed fields from the super-resolved input with $\alpha = 16$ are shown in figure 13(a). The reconstructed field from the bicubic inputs is very blurry and does not contain finer structures, especially in the wake region. In contrast, the reconstructed field from the machine-learning-based super-resolved data is in reasonable agreement with reference DNS, which implies that the accuracy of input super-resolved fields affects directly the reconstruction accuracy of the three-dimensional flow field.

We also assess the relationship between the reconstruction L_2 error and data compression ratio in each case of α , in figure 13(b). The advantage of the use of machine-learning-based super resolution can also be found with the other downsampling factor. Noteworthy here is that there is almost no difference between the cases with sectional data with $\alpha = 8$ and original DNS data, which can achieve approximately 1/2000 compression against the original data as presented as the red curve in figure 13(b). Users can choose an appropriate factor while caring about the trade-off relationship among the reconstruction error, the computational storage, and the training cost for machine learning models.

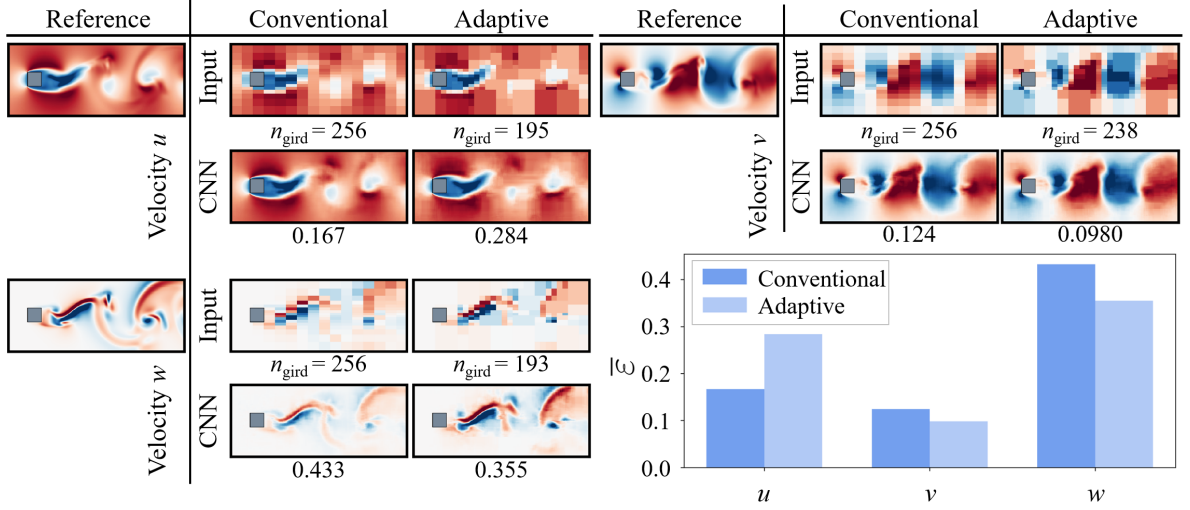


Figure 14: Super-resolution reconstruction from adaptive sampled coarse data. The values underneath the contours of input indicate the number of grid points. The values below the contours indicate the L_2 error norm. The relationship between the sampling method and the L_2 error norm depending on the velocity attributes is also shown.

3.2.2. Combination with adaptive sampling

As introduced in section 2.2, we further aim to achieve more efficient data handling with adaptive sampling. Again, the adaptive sampling enables us to generate low-resolution data based on the difference in the ‘importance’ of each arbitrary region. We summarize the application of two-dimensional super resolution with adaptive sampling in figure 14. Note that the considered downsampling factor α of conventional pooling in figure 14 is not same as the discussion above — $\alpha_x = 16$ in the streamwise direction and $\alpha_y = 8$ in the normal direction — in order to align the number of grid points with adaptive sampling $n_{\text{grid,adaptive}}$ as possible as we can. The reconstruction accuracy with the present adaptive sampling for v and w components is superior to that of conventional average pooling while reducing the number of grids. Especially, the number of grid points for w component can be saved approximately 75% against that with conventional pooling. However, we should caution that the use of adaptive sampling does not work well for the u component in this particular example. It is caused by difficulty in determining the universal weight through the convolutional operation for the velocity component which structures significantly vary over each snapshot. This implies that care should be taken for the choice of an appropriate pooling method depending on data that users handle. In turn, it also enables us to notice that there may be an optimal combination of pooling methods and their sampling ratio so as to achieve efficient data saving.

Finally, let us exemplify the hybrid method of conventional pooling and adaptive sampling, by presenting the three-dimensional reconstruction in figure 15. For this investigation, we use $n_{\text{sections}} = 5$ for all models. The hybrid pooling here represents that the conventional pooling is used for the u component while taking the adaptive sampling for the v and w components. As shown, the hybrid utilization can achieve almost same error label as that with conventional pooling while saving the storage to approximately

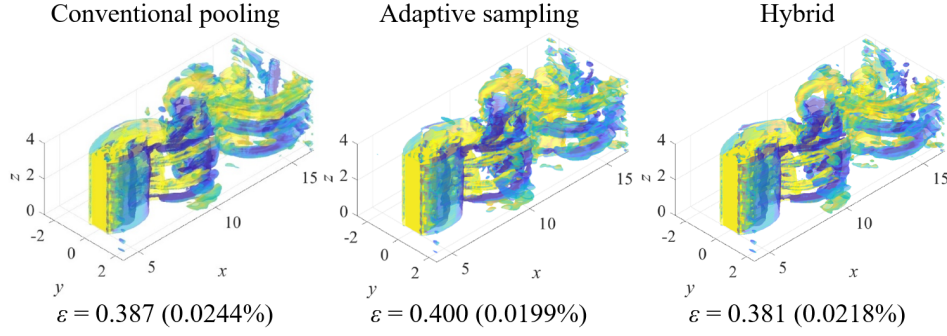


Figure 15: Three-dimensional reconstructed fields from coarse input combining the conventional pooling and the adaptive sampling. Listed values indicate the L_2 error and the compression ratio against the number of grid points over the original three-dimensional discretized domain.

0.0218% against the original number of grid points. This hybrid method can also be combined with sophisticated tools to determine optimal pooling ratio for adaptive sampling, e.g., hyperopt [39] and Bayesian optimization [40].

4. Concluding remarks

We proposed a method to reconstruct a three-dimensional flow field from its sectional data using a convolutional neural network (CNN). The present model was tested with a flow around a square cylinder at $Re_D = 300$. The proposed model referred to as 2D-3D CNN can achieve a reasonable reconstruction from few sections in terms of both the visualization assessments and the qualitative examinations. We additionally found that the model trained with as little as $n_{\text{snapshot}} = 50$ was able to capture large scale structures of fluid flows. Considering the application of the present model to experimental situations, the response of the model against noisy input was also investigated, which shows promising robustness.

As a further assessment from the aspect of data compression, we combined the three-dimensional reconstruction model with two-dimensional super-resolution analysis. Before combining with the present model, we assessed the super resolution for two-dimensional velocity fields itself. The CNN-based super resolution was superior to the bicubic interpolation in terms of estimation accuracy. The super-resolved sectional data was then fed into the pre-trained model for three-dimensional reconstruction. The case using super-resolved sectional data with downsampling factor $\alpha = 8$ can achieve almost same error level as that using original two-dimensional velocity data, which corresponds to approximately 1/2000 compression against the original data.

Moreover, we also suggested adaptive sampling which can efficiently downsample data while accounting for the importance of the data to generate a low-resolution field. In the present example, the reconstructions for v and w components with adaptive sampling-based super resolution were superior to that with the conventional average pooling while being able to reduce the number of grid points, i.e., storage of the data. For different problems, however, care should be taken for the choice of an appropriate pooling method depending on data users handle.

We finally discuss considerable extensions and remaining issues of our proposal. One of them is an application to turbulence, although this is extremely challenging as compared to the present demonstration with the square cylinder wake. To that end, we may be able to capitalize on the idea of autoencoder-based low dimensionalization [49], in addition to the present adaptive sampling. But we should caution that there may be a trade-off relationship between the compressibility and explainability of low-dimensionalized representation. Another considerable limitation is the application to unstructured mesh data which can be seen in handling complex fluid flow data. This limitation is caused by the use of regular CNN in the present study. Hence, the combination with the state of the arts, e.g., Graph CNN [50], PointNet [51], PhyGeoNet [52], and Voronoi CNN [53], may help us to tackle that issue. Moreover, what we should solve toward practical applications is how to believe results generated by machine learning model since we must encounter the situation where we have no solution data in real-life applications. In this sense, a preparation for proper uncertainty quantification [54] needs to be established. We hope that the present study can serve as one of the pieces toward effective data handling with machine learning for complex nonlinear systems.

Acknowledgement

This work was supported from Japan Society for the Promotion of Science (KAKENHI grant number: 18H03758). The authors thank Mr. Hikaru Murakami (Keio University) for sharing his DNS data.

Appendix A: Visualization at $y - z$ and $x - z$ cross sections

We here present the reconstructed velocity fields with the present CNN model at the $y - z$ and $x - z$ cross sections in figure 16. As reported with the $x - y$ sections and three-dimensional visualization in figures 7 and 8, the present model can reconstruct the flow field with reasonable accuracy. The difference of the estimation accuracy among the velocity components can be explained with their complexities observed in figure 9.

Appendix B: Gradient difference loss

For the construction of the present models above, we choose mean squared error (MSE) as the loss function. We here discuss the influence of the reconstruction results on the choice of loss function. In addition to the use of MSE, we consider two types of customized function; the combination of MSE with 1: a forward difference gradient difference loss (GDL) referred to as GDL_1 and 2: a central difference GDL referred to as GDL_2 . It is widely known that containing the GDL into a loss function enables us to achieve smooth fluid flow reconstructions [12, 13, 55, 56]. The covered loss functions can be expressed as,

$$\text{MSE} = \frac{1}{N_\phi} \frac{1}{N_z^\#} \frac{1}{N_y^\#} \frac{1}{N_x^\#} \sum_{l=1}^{N_\phi} \sum_{k=1}^{N_z^\#} \sum_{j=1}^{N_y^\#} \sum_{i=1}^{N_x^\#} (q_{\text{DNS},(i,j,k,l)} - (q_{\text{ML},(i,j,k,l)}))^2, \quad (7)$$

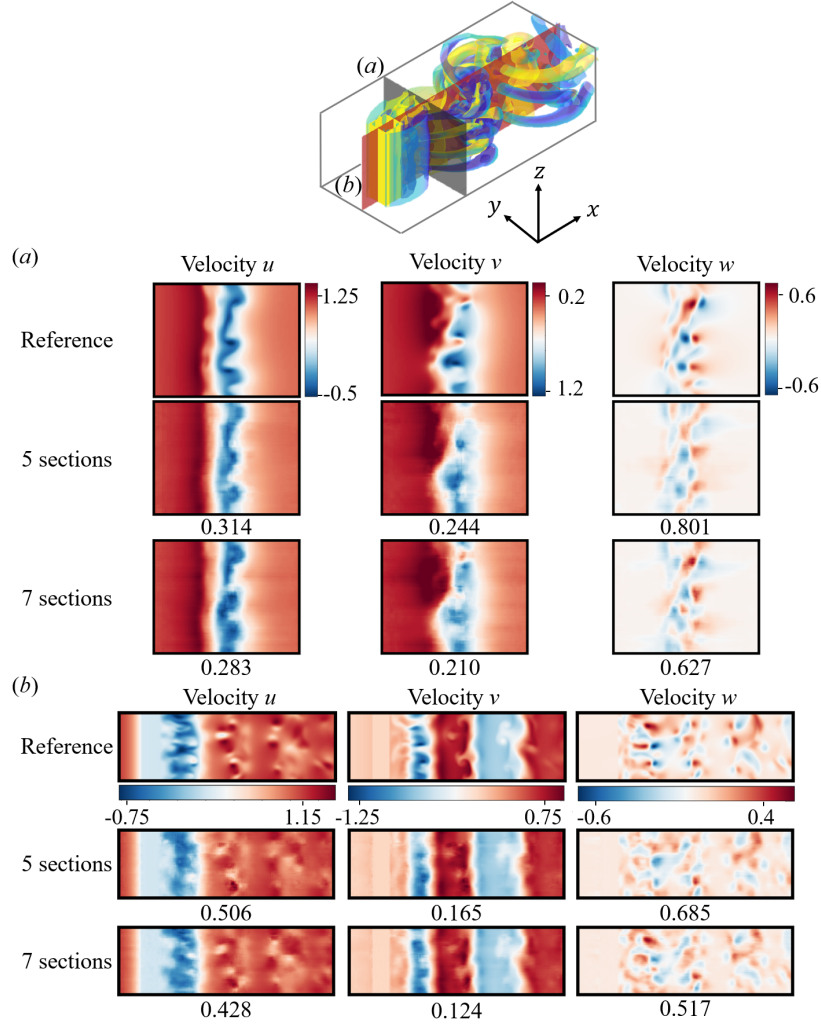


Figure 16: Reconstructed velocity fields by the present CNN model with $n_{\text{section}} = 5$ and 7. (a) $y-z$ cross section at $\Delta x/D = 8$. (b) $x-z$ cross section at $\Delta y/D = 0$. The values underneath contours are the L_2 error norm.

$$\begin{aligned}
\text{GDL}_1 &= \frac{1}{N_\phi} \frac{1}{N_z^\#} \frac{1}{N_y^\#} \frac{1}{N_x^\#} \sum_{l=1}^{N_\phi} \sum_{k=1}^{N_z^\#} \sum_{j=1}^{N_y^\#} \sum_{i=1}^{N_x^\#} \\
&\quad \left(|q_{\text{DNS},(i+1,j,k,l)} - q_{\text{DNS},(i,j,k,l)}| - |q_{\text{ML},(i+1,j,k,l)} - q_{\text{ML},(i,j,k,l)}| \right) \\
&+ \left(|q_{\text{DNS},(i,j+1,k,l)} - q_{\text{DNS},(i,j,k,l)}| - |q_{\text{ML},(i,j+1,k,l)} - q_{\text{ML},(i,j,k,l)}| \right) \\
&+ \left(|q_{\text{DNS},(i,j,k+1,l)} - q_{\text{DNS},(i,j,k,l)}| - |q_{\text{ML},(i,j,k+1,l)} - q_{\text{ML},(i,j,k,l)}| \right),
\end{aligned} \tag{8}$$

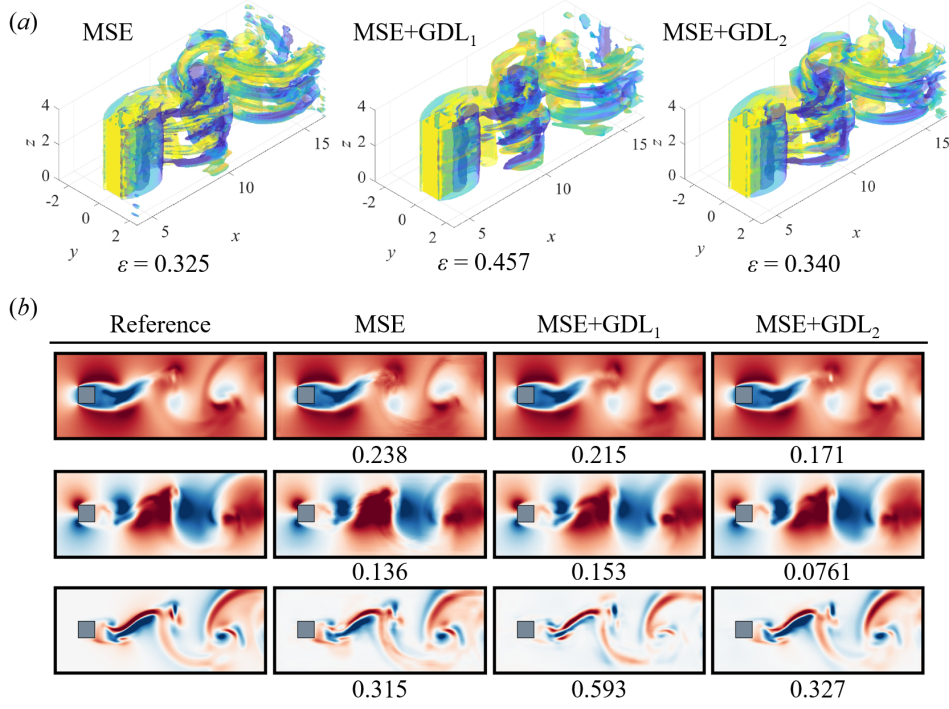


Figure 17: Choice of loss function for the present CNN model. (a) Three-dimensional visualization of the reconstructed flow field. (b) Reconstructed sectional velocities at $\Delta z/D = 0.025$. The values underneath fields are the L_2 error norm.

$$\begin{aligned}
\text{GDL}_2 = & \frac{1}{N_\phi} \frac{1}{N_z^\#} \frac{1}{N_y^\#} \frac{1}{N_x^\#} \sum_{l=1}^{N_\phi} \sum_{k=1}^{N_z^\#} \sum_{j=1}^{N_y^\#} \sum_{i=1}^{N_x^\#} \\
& \left(\left| (q_{\text{DNS},(i+1,j,k,l)} - q_{\text{DNS},(i,j,k,l)}) + (q_{\text{DNS},(i-1,j,k,l)} - q_{\text{DNS},(i,j,k,l)}) \right| \right. \\
& - \left. \left| (q_{\text{ML},(i+1,j,k,l)} - q_{\text{ML},(i,j,k,l)}) + (q_{\text{ML},(i-1,j,k,l)} - q_{\text{ML},(i,j,k,l)}) \right| \right) \\
& + \left(\left| (q_{\text{DNS},(i,j+1,k,l)} - q_{\text{DNS},(i,j,k,l)}) + (q_{\text{DNS},(i,j-1,k,l)} - q_{\text{DNS},(i,j,k,l)}) \right| \right. \\
& - \left. \left| (q_{\text{ML},(i,j+1,k,l)} - q_{\text{ML},(i,j,k,l)}) + (q_{\text{ML},(i,j-1,k,l)} - q_{\text{ML},(i,j,k,l)}) \right| \right) \\
& + \left(\left| (q_{\text{DNS},(i,j,k+1,l)} - q_{\text{DNS},(i,j,k,l)}) + (q_{\text{DNS},(i,j,k-1,l)} - q_{\text{DNS},(i,j,k,l)}) \right| \right. \\
& - \left. \left| (q_{\text{ML},(i,j,k+1,l)} - q_{\text{ML},(i,j,k,l)}) + (q_{\text{ML},(i,j,k-1,l)} - q_{\text{ML},(i,j,k,l)}) \right| \right),
\end{aligned} \tag{9}$$

where N_ϕ is the number of physical quantity. There are three velocity components $\{u, v, w\}$ in this study such that $N_\phi = 3$.

The influence on the choice of loss function is summarized in figure 17. Although the L_2 error becomes a bit worse, the reconstructed field with GDL₂ shows smoother vortical

structures than that with MSE, as presented in figure 17(a). Although since its effect relies on the flow attributes as shown in figure 17(b), users may benefit depending on their purposes.

References

- [1] E. Moore, G., Cramming more components onto integrated circuits, *Electronics* 38 (1965) 1–4.
- [2] T. Kajishima, K. Taira, *Computational fluid dynamics*, Cham: Springer International Publishing (1).
- [3] S. L. Brunton, B. R. Noack, P. Koumoutsakos, Machine learning for fluid mechanics, *Annu. Rev. Fluid Mech.* 52 (2020) 477–508.
- [4] J. N. Kutz, Deep learning in fluid dynamics, *J. Fluid Mech.* 814 (2017) 1–4.
- [5] S. L. Brunton, M. S. Hemanti, K. Taira, Special issue on machine learning and data-driven methods in fluid dynamics, *Theor. Comput. Fluid Dyn.* 34 (4) (2020) 333–337.
- [6] K. Taira, M. S. Hemati, S. L. Brunton, Y. Sun, K. Duraisamy, S. Bagheri, S. Dawson, C.-A. Yeh, Modal analysis of fluid flows: Applications and outlook, *AIAA J.* 58 (3) (2020) 998–1022.
- [7] M. P. Brenner, J. D. Eldredge, J. B. Freund, Perspective on machine learning for advancing fluid mechanics, *Phys. Rev. Fluids* 4 (2019) 100501.
- [8] G. E. Hinton, R. R. Salakhutdinov, Reducing the dimensionality of data with neural networks, *Science* 313 (5786) (2006) 504–507.
- [9] M. Milano, P. Koumoutsakos, Neural network modeling for near wall turbulent flow, *J. Comput. Phys.* 182 (2002) 1–26.
- [10] T. Murata, K. Fukami, K. Fukagata, Nonlinear mode decomposition with convolutional neural networks for fluid dynamics, *J. Fluid Mech.* 882 (2020) A13.
- [11] K. Fukami, T. Nakamura, K. Fukagata, Convolutional neural network based hierarchical autoencoder for nonlinear mode decomposition of fluid field data, *Phys. Fluids* 32 (2020) 095110.
- [12] K. Hasegawa, K. Fukami, T. Murata, K. Fukagata, Machine-learning-based reduced-order modeling for unsteady flows around bluff bodies of various shapes, *Theor. Comput. Fluid Dyn.* 34 (4) (2020) 367–388.
- [13] K. Hasegawa, K. Fukami, T. Murata, K. Fukagata, CNN-LSTM based reduced order modeling of two-dimensional unsteady flows around a circular cylinder at different Reynolds numbers, *Fluid Dyn. Res.* 52 (2020) 065501.

- [14] K. Hasegawa, K. Fukami, T. Murata, K. Fukagata, Data-driven reduced order modeling of flows around two-dimensional bluff bodies of various shapes, ASME-JSME-KSME Joint Fluids Engineering Conference, San Francisco, USA (Paper 5079).
- [15] T. Nakamura, K. Fukami, K. Hasegawa, Y. Nabae, K. Fukagata, Convolutional neural network and long short-term memory based reduced order surrogate for minimal turbulent channel flow, *Phys. Fluids* 33 (2021) 025116.
- [16] K. Fukami, T. Murata, K. Fukagata, Sparse identification of nonlinear dynamics with low-dimensionalized flow representations, *arXiv:2010.12177*.
- [17] J. Xu, K. Duraisamy, Multi-level convolutional autoencoder networks for parametric prediction of spatio-temporal dynamics, *Comput. Methods Appl. Mech. Eng.* 372 (2020) 113379.
- [18] R. Maulik, B. Lusch, P. Balaprakash, Reduced-order modeling of advection-dominated systems with recurrent neural networks and convolutional autoencoders, *arXiv:2002.00470*.
- [19] Y. Liu, C. Ponce, S. L. Brunton, J. N. Kutz, Multiresolution convolutional autoencoders, *arXiv:2004.04946*.
- [20] N. B. Erichson, M. Muehlebach, M. W. Mahoney, Physics-informed autoencoders for lyapunov-stable fluid flow prediction, *arXiv:1905.10866*.
- [21] N. Omata, S. Shirayama, A novel method of low-dimensional representation for temporal behavior of flow fields using deep autoencoder, *AIP Adv.* 9 (1) (2019) 015006.
- [22] B. Lusch, J. N. Kutz, S. L. Brunton, Deep learning for universal linear embeddings of nonlinear dynamics, *Nature Comm.* 9 (1) (2018) 4950.
- [23] A. Glaws, R. King, M. Sprague, Deep learning for in situ data compression of large turbulent flow simulations, *Phys. Rev. Fluids* 5 (2020) 114602.
- [24] M. Morimoto, K. Fukami, K. Zhang, A. G. Nair, K. Fukagata, Convolutional neural networks for fluid flow analysis: toward effective metamodeling and low-dimensionalization, *arXiv:2101.02535*.
- [25] N. B. Erichson, L. Mathelin, Z. Yao, S. L. Brunton, M. W. Mahoney, J. N. Kutz, Shallow neural networks for fluid flow reconstruction with limited sensors, *Proc. Royal Soc. A* 476 (2238) (2020) 20200097.
- [26] K. Fukami, K. Fukagata, K. Taira, Assessment of supervised machine learning for fluid flows, *Theor. Comput. Fluid Dyn.* 34 (4) (2020) 497–519.
- [27] K. Fukami, K. Fukagata, K. Taira, Super-resolution reconstruction of turbulent flows with machine learning, *J. Fluid Mech.* 870 (2019) 106–120.
- [28] K. Fukami, K. Fukagata, K. Taira, Super-resolution analysis with machine learning for low-resolution flow data, in: 11th International Symposium on Turbulence and Shear Flow Phenomena (TSFP11), Southampton, UK, no. 208, 2019.

- [29] K. Fukami, K. Fukagata, K. Taira, Machine learning based spatio-temporal super resolution reconstruction of turbulent flows, *J. Fluid Mech.* 909 (2021) A9.
- [30] Y. LeCun, L. Bottou, Y. Bengio, P. Haffner, Gradient-based learning applied to document recognition, *Proc. IEEE* 86 (11) (1998) 2278–2324.
- [31] Y. LeCun, Y. Bengio, G. Hinton, Deep learning, *Nature* 521 (2015) 436–444.
- [32] K. Fukami, Y. Nabae, K. Kawai, K. Fukagata, Synthetic turbulent inflow generator using machine learning, *Phys. Rev. Fluids* 4 (2019) 064603.
- [33] K. Champion, B. Lusch, J. N. Kutz, S. L. Brunton, Data-driven discovery of coordinates and governing equations, *Proc. Natl. Acad. Sci.* 45 (116).
- [34] B. Liu, J. Tang, H. Huang, X.-Y. Lu, Deep learning methods for super-resolution reconstruction of turbulent flows, *Phys. Fluids* 32 (2020) 025105.
- [35] J. Kim, C. Lee, Prediction of turbulent heat transfer using convolutional neural networks, *J. Fluid Mech.* 882 (2020) A18.
- [36] M. Morimoto, K. Fukami, K. Fukagata, Experimental velocity data estimation for imperfect particle images using machine learning, *arXiv:2005.00756*.
- [37] K. He, Z. X., S. Ren, J. Sun, Deep residual learning for image recognition., *Proc. IEEE* (2016) 770–778.
- [38] V. Nair, G. E. Hinton, Rectified linear units improve restricted boltzmann machines, *Proc. Int. Conf. Mach. Learn.* (2010) 807–814.
- [39] J. Bergstra, D. Yamins, D. Cox, Making a science of model search: Hyperparameter optimization in hundreds of dimensions for vision architectures, in: *International conference on machine learning*, PMLR, 2013, pp. 115–123.
- [40] R. Maulik, A. Mohan, B. Lusch, S. Madireddy, P. Balaprakash, D. Livescu, Time-series learning of latent-space dynamics for reduced-order model closure, *Physica D: Nonlinear Phenomena* 405 (2020) 132368.
- [41] L. Prechelt, Automatic early stopping using cross validation: quantifying the criteria, *Neural Netw.* 11 (4) (1998) 761–767.
- [42] S. L. Brunton, J. N. Kutz, *Data-Driven Science and Engineering: Machine Learning, Dynamical Systems, and Control*, Cambridge University Press (2019) ISBN, 1108422098.
- [43] H. Bai, M. M. Alam, Dependence of square cylinder wake on reynolds number, *Phys. Fluids* 30 (2018) 015102.
- [44] J. P. Caltagirone, Sur l’interaction fluide-milieu poreux: application au calcul des efforts excersés sur un obstacle par un fluide visqueux, *C. R. Acad. Sci. Paris* 318 (1994) 571–577.

- [45] J. Jeong, F. Hussian, On the identification of a vortex, *J. Fluid Mech.* 285 (1995) 69–94.
- [46] J. M. Pérez, S. L. Clainche, J. M. Vega, Reconstruction of three-dimensional flow fields from two-dimensional data, *J. Comput. Phys.* 407 (2020) 109239.
- [47] M. Morimoto, K. Fukami, K. Zhang, K. Fukagata, Generalization techniques of neural networks for fluid flow estimation, *arXiv:2011.11911*.
- [48] R. Keys, Cubic convolution interpolation for digital image processing, *IEEE transactions on acoustics, speech, and signal processing* 29 (6) (1981) 1153–1160.
- [49] K. Fukami, K. Hasegawa, T. Nakamura, M. Morimoto, K. Fukagata, Model order reduction with neural networks: Application to laminar and turbulent flows, *arXiv:2011.10277*.
- [50] F. Ogoke, K. Meidani, A. Hashemi, A. B. Farimani, Graph convolutional neural networks for body force prediction, *arXiv:2012.02232*.
- [51] A. Kashefi, D. Rempe, L. J. Guibas, A point-cloud deep learning framework for prediction of fluid flow fields on irregular geometries, *Phys. Fluids* 33 (2021) 027104.
- [52] H. Gao, L. Sun, J.-X. Wang, PhyGeoNet: Physics-Informed Geometry-Adaptive Convolutional Neural Networks for Solving Parameterized Steady-State PDEs on Irregular Domain, *J. Comput. Phys.* (2020) 110079.
- [53] K. Fukami, R. Maulik, N. Ramachandra, K. Fukagata, K. Taira, Global field reconstruction from sparse sensors with Voronoi tessellation-assisted deep learning, *arXiv:2101.00554*.
- [54] R. Maulik, K. Fukami, N. Ramachandra, K. Fukagata, K. Taira, Probabilistic neural networks for fluid flow surrogate modeling and data recovery, *Phys. Rev. Fluids* 5 (2020) 104401.
- [55] M. Mathieu, C. Couprie, Y. LeCun, Deep multi-scale video prediction beyond mean square error, *arXiv:1511.05440v6*.
- [56] S. Lee, D. You, Data-driven prediction of unsteady flow fields over a circular cylinder using deep learning, *J. Fluid Mech.* 879 (2019) 217–254.